International Journal of Mass Spectrometry 303 (2011) 154–163

Contents lists available at ScienceDirect

International Journal of Mass Spectrometry

journal homepage: www.elsevier.com/locate/ijms

Gas-phase ion dynamics in a periodic-focusing DC ion guide (Part II): Discrete transport modes

Chaminda M. Gamage, Joshua A. Silveira, Ryan C. Blase, David H. Russell*

Texas A&M University, Department of Chemistry, Laboratory for Biological Mass Spectrometry, College Station, TX 77843, United States

ARTICLE INFO

Article history:
Received 9 November 2010
Received in revised form 24 January 2011
Accepted 24 January 2011
Available online 2 February 2011

Keywords:
Ion mobility spectrometry
Collision cross section
Ion guide
Periodic focusing
Effective potential
Pseudopotential

ABSTRACT

The purpose of this work is to expand on the theory presented by Silveira et al. [*Silveira et al., International Journal of Mass Spectrometry 296 (2010) 36–42*], to include a detailed discussion of discrete ion transport properties in the periodic-focusing DC ion guide (PDC IG) that result in radial ion focusing and ion mobility. We previously noted that although the PDC IG utilizes only electrostatic fields, ions are subjected to an effective RF as they traverse the device in the axial (z) direction. Here, the radial electric field (E_r) oscillations generating the effective RF are investigated in detail. Equations of motion are derived to explain ion movement in the radial (r) direction. The results suggest that a collisionally dampened effective potential (V^*) model can explain the observed radial ion confinement. Furthermore, a mathematical explanation regarding the effects of the non-uniform axial electric field and periodic collisional cooling phenomena generated in the PDC IG is presented in the context of ion mobility spectrometry (IMS). Included is a detailed discussion of the ion mobility coefficient (K), ion mobility resolution (R), and subsequent determination of the ion-neutral collision cross section (Ω) using the PDC IG. The results indicate that the PDC IG affords straightforward and accurate determination of K and Ω *via* incorporation of a mobility damping coefficient (α) which is easily derived based upon the operating conditions and the electrode geometry.

1. Introduction

Radial diffusion adversely affects the analytical figures-of-merits in ion mobility spectrometry (IMS), specifically ion transmission, which imposes severe limitations on the overall instrument sensitivity. Several approaches which correct for radial diffusion have been attempted including positioning the drift tube in a strong magnetic field [1], incorporating RF ion funnels [2], periodic-focusing DC ion guides (PDC IGs) [3,4], RF stacked ring drift tubes [5] and traveling wave devices [6,7]. Although each of these approaches has demonstrated increased ion transmission, all come at the expense of other analytical figures-of-merit, such as extensive calibration methods, decreased IMS resolution, uncertainty in the effective ion temperature (T_{eff}), and decreased accuracy of collision cross section (Ω) measurements.

In this work, we expand upon the gas-phase ion dynamics of the PDC IG presented in reference [8] to include a detailed description of the radial (r) and axial (z) ion transport properties that result in ion focusing and ion mobility separation, respectively. Previously, we demonstrated that the PDC IG contains the properties of an ion guide and an ion mobility spectrometer yielding high ion transmission and high resolution ($R \sim 50$–120 for singly charged ions) IMS separations [4,9]. In terms of radial ion focusing, several key features of the PDC IG have been realized: (1) ions with a given axial velocity (V_z) are subjected to an effective RF as they traverse the device owing to the spatial periodicity of the radial electric field, E_r, (2) the magnitude of E_r varies as a function of the r-dimension, (3) under stable operating conditions, compensation for radial diffusion is indicative of a focusing mechanism operating on the basis of effective potentials analogous to RF devices [10,11], and (4) T_{eff} varies as a function of z-position initiated by the variations in the axial electric field (E_z) [8]. Results (1–3) are analogous to the focusing properties of a stacked-ring DC ion guide (DC IG) reported by Guan and Marshall [12], whereas property (4) remains unique to the PDC IG operating at elevated pressures ~1–5 Torr.

The term effective RF refers to the spatial changes of the static E_r encountered by an ion traversing the PDC IG in the z-direction with a given velocity. This scenario is inverse to traditional RF but ultimately creates an analogous effect. While the effective RF generates an apparent defocusing and a subsequent focusing effect in a single electrode subunit, the net drift of an ion trajectory towards the central $r = 0$ position over several RF cycles is attributed to the presence

* Corresponding author at: Texas A&M University, Interdisciplinary Life Sciences Building, 3474 TAMU, College Station, TX 77843-3474, United States.
Tel.: +1 979 845 3345; fax: +1 979 845 9485.
E-mail address: russell@chem.tamu.edu (D.H. Russell).

1387-3806/$ – see front matter © 2011 Elsevier B.V. All rights reserved.
doi:10.1016/j.ijms.2011.01.025

of effective potentials. Moreover, the middle region of the PDC IG electrodes acts as a collisional cooling region owing to an increase in the number of ion-neutral collisions per unit z-displacement (n) initiated by the axial electric field, E_z, oscillations. Collisional cooling assists the effective potentials at the tailing edge of the electrode by slowly focusing ions towards the central drift axis. Compared to conventional drift time based uniform field IMS (DT IMS) coupled to mass spectrometry (MS), the PDC IG-MS design allows for a substantial (up to 40-fold) increase in ion transmission accompanied by a modest (~10%) decrease in the IMS resolving power, depending on the experimental conditions and the drift tube design [9]. Here, the discussion of radial motion is extended with an emphasis on clarifying the role of effective RF which facilitates radial ion focusing and utilization of the PDC IG as a high transmission ion mobility spectrometer. A mathematical treatment for effective RF ion motion is presented and the generation of effective potentials from radial variations of the effective RF is discussed along with collisional damping effects.

In addition, the axial ion transport mode is investigated in terms of ion mobility separation. Recently, IMS has become an important platform for the elucidation of 3D structures and their changes in polyatomic frameworks including ionic clusters [13–17], metal–ligand complexes [18,19], peptide ions [20–22] as well as protein ions [23–27]. Traditionally, the ion-neutral cross section (Ω) is obtained by DT IMS whereby ions traverse a drift tube of length L filled with a neutral buffer gas under the influence of a uniform electric field (E) such that the mobility coefficient (K) is given by [28],

$$K = \frac{L}{t_d E} \tag{1}$$

where t_d is the drift time of the ion in the drift tube. K may also be expressed as the reduced ion mobility coefficient, K_0, obtained by standardizing K to standard temperature and pressure,

$$K_0 = K\frac{P}{P_0}\frac{T_0}{T} \tag{2}$$

where P is the drift gas pressure, P_0 is the standard pressure, T is the drift gas temperature, and T_0 is the standard temperature. Structural features may be deduced using the parameters K_0 and Ω expressed in the relationship [28,29],

$$K_0 = \left(\frac{3q}{16N_0}\right)\left(\frac{2\pi}{\mu K_B T}\right)^{1/2}\left(\frac{1}{\Omega}\right) \tag{3}$$

where,

$$\mu = \frac{mM}{m+M} \tag{4}$$

The terms N_0, m, M, q and μ represent the standard particle number density of the buffer gas, the mass of the ion, the mass of the buffer gas, the charge of the ion and the reduced mass, respectively. While K offers information on relative differences between structures, Ω provides additional detail on the overall size and shape of the ions. From Eqs. (1)–(3), Ω can be obtained from the expression,

$$\Omega = \left(\frac{3q}{16N_0}\right)\left(\frac{2\pi}{\mu K_B T}\right)^{1/2}\left(\frac{t_D E}{L}\right)\left(\frac{P_0 T}{P T_0}\right) \tag{5}$$

The accuracy of K measured by DT IMS for the subsequent calculation of Ω using Eq. (5) depends critically on the experimental and instrumental parameters employed, *viz.* E, P, T and other factors which affect the arrival time distribution. In addition, while t_D measured at the peak centroid (assuming a single conformation) is sufficient for obtaining K and Ω, the resolution of the technique (R) becomes increasingly important when multiple analytes and/or structural conformations with similar mobility are present. In DT IMS, the diffusion-limited resolution (R) is given by,

$$R = \frac{t_d}{\Delta t_d} = \frac{1}{4}\left(\frac{qLE}{K_B T\ \ln 2}\right)^{1/2} \tag{6}$$

where Δt_d is the full width of the mobility peak at half maximum height. Previous IMS-MS studies by Sawyer et al. on the structure of gas-phase bradykinin fragment 1-5 revealed three distinct conformations of the peptide *via* IMS measurement with a PDC IG and calibration procedures assuming first-order IMS principles [30]. In this work, we also provide theoretical validation for the aforementioned method and discuss the specific impacts of instrumental parameters including the spatial variations of the axial electric field, E_z, and the periodic collisional cooling effects represented by n, the number of ion-neutral collisions per unit z-displacement, for the determination of K, R, and Ω in the PDC IG.

2. Experimental

2.1. Chemicals and samples

A fullerene mixture (C_{60} and C_{70}) and benzene were purchased from Sigma–Aldrich (St. Louis, MO). A suspension of fullerene in benzene was deposited on a stainless steel sample probe and allowed to dry prior to analysis.

2.2. Instrumentation

Instrumentation used in this study has been described previously [9]. Briefly, two L = 63 cm PDC IG designs were constructed with different electrode geometries. The ratio between electrode spacing (s), electrode width (w) was kept constant while the inner diameter (d) of the electrode was varied. Specifically, both designs utilized $s = w$ = 6 mm while d was varied: 6 mm (s:w:d ratio = 1:1:1) and 8 mm (s:w:d ratio = 3:3:4). A voltage drop was established with a series of 1 MΩ resistors connecting adjacent electrodes. The maximum voltage drop (V) across both designs was ~3500 V. Samples were spotted on a stainless steel probe and inserted into the drift cell between the first and second electrode. A nitrogen laser, λ = 337 nm (Stanford Research Systems, Sunnyvale, CA), was used to create ions *via* laser desorption ionization. The drift tube pressure was maintained between 1 and 3 Torr with He buffer gas. A 500 μm aperture was placed at the exit of each PDC IG to aid in differential pumping for ion detection with a Galileo Channeltron electron multiplier (CEM) detector (Burle Electro-Optics, Inc.; Lancaster, PA).

2.3. Ion optics simulations

For detailed descriptions of the methods used in the derivation of electric fields or simulation of ion trajectories, the reader is referred to reference [8]. Briefly, ion-neutral collisional dynamics were simulated for both periodic-focusing lens geometries using $C_{60}^{\bullet+}$ ions (720 m/z, Ω = 124 Å^2) and He buffer gas with a user program provided with SIMION 8.0 (*collision_hs1.lua*) to include ion-neutral hard sphere elastic collisions at 300 K.

2.4. Drift time measurements

For the experimental determination of drift times, ion mobility spectra were obtained at varied applied electric field conditions (15–30 V cm^{-1}) at a fixed pressure between 1 and 2.5 Torr to construct arrival time (y-axis) versus $1/E$ (x-axis) plots. Each plot displayed a linear trendline with $R^2 > 0.99$. The y-intercept of the plot provided the time offset (equivalent to the time ions spend outside of the drift cell) that was subtracted from the observed arrival time in order to obtain the drift time used in the collision cross section calculations.

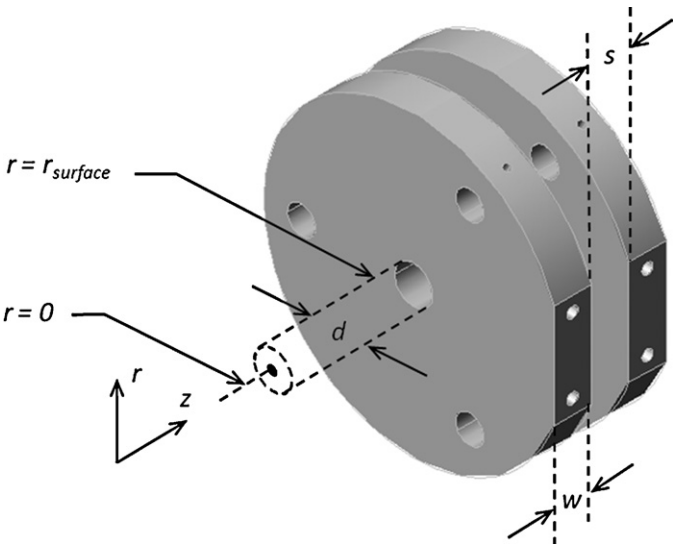

Fig. 1. Two adjacent PDC IG electrodes showing the variables that define the aspect ratio (s:w:d) and the radial (r) and axial (z) dimensions. The location of electric field boundary conditions, $r = 0$ and $r = r_{surface}$, are also indicated.

3. Results and discussion

3.1. Ion transport modes

We previously proposed an ion focusing mechanism by which the PDC IG operates and compared the properties of the device to the DC IG [8]. However, the DC IG and PDC IG differ in terms of optimum operating conditions. That is, the PDC IG contains an additional superimposed potential drop to allow for ion transport at elevated pressure and IMS separation on the basis of collision cross section. Conversely, stable operation of the DC IG requires low pressure or vacuum conditions as ion focusing resembles an extended Einzel lens system. In this work, we seek to elucidate the specific relationships between electric field profiles and radial ion focusing in PDC IG.

Fig. 1 contains a schematic representation of two lens elements in a PDC IG, including labels of the geometric variables and the cylindrical coordinate system referred to in this discussion. Fig. 2 depicts the representative trajectory of a single off-axis ion demonstrating that under stable operating conditions, overall ion motion can be decoupled into three separate channels: (1) axial drift, (2) radial ripple, and (3) central drift about $r = 0$. Axial drift motion is a result of the overall potential drop across the device giving rise to E_z which oscillates about a central value (E_c). Axial drift motion is governed by IMS relationships as discussed later in Sections 3.5 and 3.6. Moreover, our previous work introduced the concept of effective RF caused by the radial electric field variation for an ion traveling with a given V_z. While RF in multipolar ion guides and traps traditionally consider an ion at rest with respect to fast RF electrodynamic fields, an effective RF is generated by the inverse scenario: an ion moving relatively fast with respect to position-dependent electrostatic waveforms which is the case for ions traversing the PDC IG. Ion motion due to effective RF is observed as an apparent *defocusing* ((+) r-direction) followed by a subsequent *focusing* ((−) r-direction) effect within one electrode subunit which we term *radial ripple*. Consequently, the variations in the magnitude of the effective RF in the r-direction give rise to the third transport channel observed as superimposed slow central drift acting in the (−) r-direction which we previously attributed to effective potentials (V^*). In Sections 3.2–3.4, we mathematically describe the effective RF, derive equations of motion for the boundary conditions of the radial ripple motion, and evaluate a representative V^* model for a general device operating at pressures ~ 1–5 Torr.

3.2. Mathematical description of the effective RF

In this section, we will only consider a PDC IG design with an aspect ratio s:$w = 1$ for description of the electric fields as sinusoidal functions; this treatment is optimum at an r-position < $0.25d$ where ions typically reside under stable operating conditions. Fig. 3 shows the spatial oscillations along the z-dimension for the axial electric field ($E_z(z)$) and radial electric field ($E_r(z)$) at discrete r-positions for a single electrode subunit. It is important to note that $|E_z(z)|$ oscillations are dominant compared to $|E_r(z)|$ – especially at small r values. Let us initially assume a constant V_z as changes in this variable will be considered later. For these parameters, $E_z(z)$ at constant r may be described by the time-dependent expression,

$$E_z(z) = E_{0,z} \cos(\Omega_{eff} t) + E_c \quad (7)$$

where $E_{0,z}$ is the axial electric field amplitude, Ω_{eff} is the effective RF frequency in radians, and E_c is the central electric field. Similarly, $E_r(z)$ is 90° out-of-phase from the $E_z(z)$ waveform and may be approximated by the smooth curve given by,

$$E_r(z) = E_{0,r} \sin(\Omega_{eff} t) \quad (8)$$

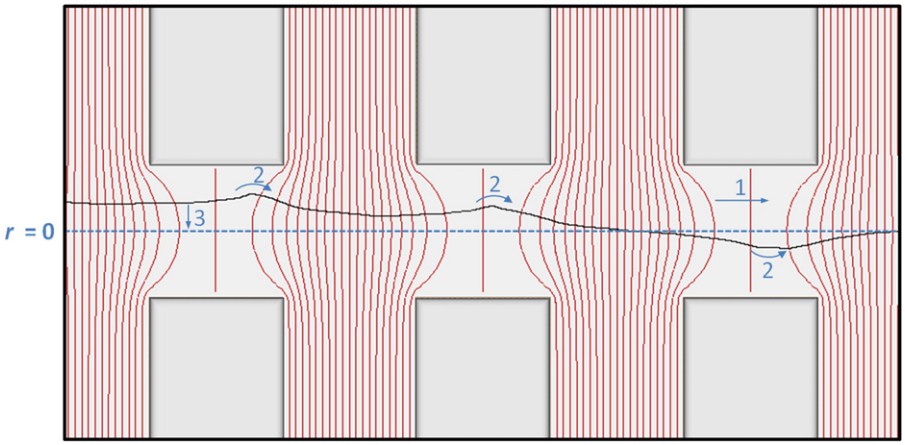

Fig. 2. Equipotential lines (shown in red) for three representative electrodes and the three major transport modes of the ion trajectory (shown in black): (1) axial drift, (2) radial ripple, and (3) central drift motion about the $r = 0$ axis (blue dashed line). In the simulation, the net electric field was 24 V cm^{-1}, the He pressure was 1 Torr, and the temperature was 300 K yielding E_c/N 75 Td. (For interpretation of the references to color in this figure legend, the reader is referred to the web version of the article.)

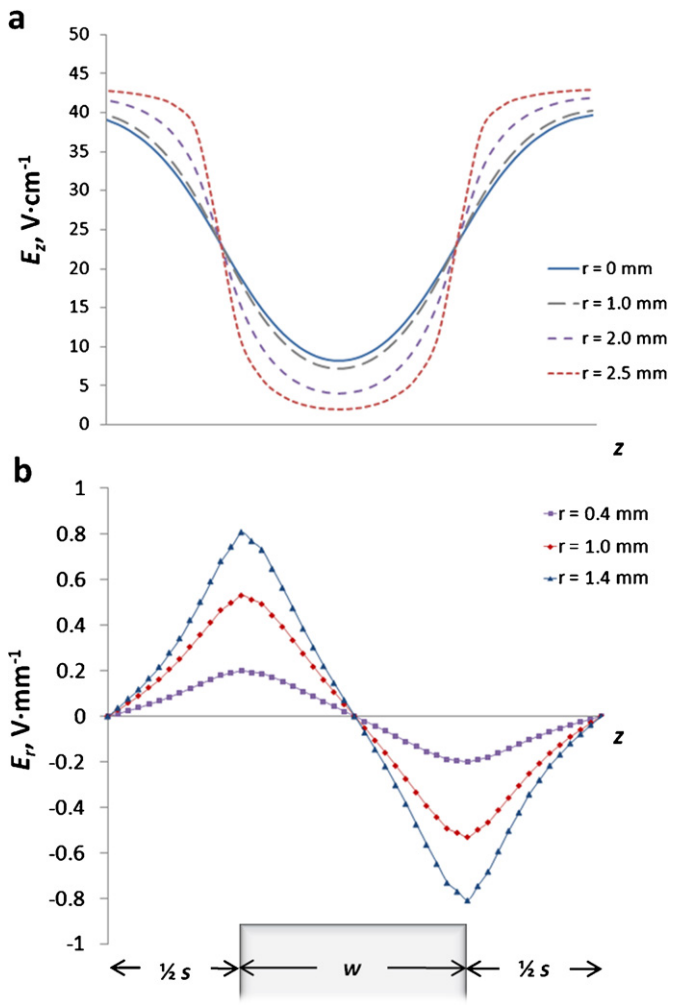

Fig. 3. Electric fields as a function of the *z*-dimension in a PDC IG: (a) axial electric field oscillations at varied *r*-position and (b) radial electric field oscillations at varied *r*-position shown for one electrode subunit. E_z directs axial ion drift while E_r generates an effective RF in the inertial frame of an ion with a given axial velocity. Analogous to RF devices, $|E_r|$ increases as *r*-position increases as illustrated in (b).

for variable radial positions with changing radial electric field amplitude, $E_{0,r}$. For the waveforms described by Eqs. (7) and (8), the wavelength (λ) is equivalent to,

$$\lambda = w + s \tag{9}$$

where w and s are the thickness and spacing of the electrodes, respectively.[1]

Moreover, the effective RF is given by,

$$\Omega_{eff} = \frac{2\pi V_z}{\lambda} \tag{10}$$

in radians [8,12]. The average effective RF ($\bar{\Omega}_{eff}$) may be calculated considering the ion depicted in Fig. 2. At E/N 75 Td the average axial ion velocity for $C_{60}^{\bullet+}$ in He is $\bar{V}_z \sim 0.83$ mm μs^{-1} corresponding to an average drift time ~380 μs over a 32 cm drift length. For 26 electrodes of dimensions $s = w = 6$ mm ($\lambda = 12$ mm), $\frac{\bar{\Omega}_{eff}}{2\pi} = 70$ kHz. Thus, although not intuitively obvious, ions in the PDC IG experience an effective RF with an average frequency in the kHz range comparable to conventional RF multipole ion guides and traps [31].

3.3. Equations of radial ion motion

The radial electric force, F_r, generating the radial ripple can be derived considering a system with constant amplitude $E_{0,r}$ (fixed *r*-position), and constant axial velocity ($\bar{V}_z$). Let us also initially assume vacuum conditions since this is defined as one boundary condition to describe the radial ion motion. Considering the harmonic field changes as a function in time,

$$F_r = ma_r = qE_r = qE_{0,r} \sin(\Omega_{eff} t) \tag{11}$$

where a_r is the radial acceleration of the ion. Rearranging Eq. (11) and substituting Eq. (10), the radial acceleration of the ion becomes,

$$a_r = \frac{q}{m} E_{0,r} \sin\left(\frac{2\pi V_z}{\lambda} t\right) \tag{12}$$

Under vacuum conditions, the radial velocity component ($V_{r,v}$) due to the effective RF motion can be obtained by integrating Eq. (12) with respect to t yielding,

$$V_{r,v} = -\frac{q}{m} E_{0,r} \left(\frac{\lambda}{2\pi V_z}\right) \cos\left(\frac{2\pi V_z}{\lambda} t\right) + V_{r,v,i} \tag{13}$$

where $V_{r,v,i}$ is the initial radial velocity in vacuum. Accordingly, displacement in the *r*-direction for vacuum conditions is obtained *via* integration of Eq. (13) with respect to t yielding,

$$r_v = -\frac{q}{m} E_{0,r} \left(\frac{\lambda}{2\pi V_z}\right)^2 \sin\left(\frac{2\pi V_z}{\lambda} t\right) + V_{r,v,i} t + r_{v,i} \tag{14}$$

where $r_{v,i}$ is the initial *r*-displacement.

However, since stable operating conditions of the PDC IG requires the presence of collisional cooling, *low-field* IMS theory must also be considered. In this case, macroscopic radial drift is induced by microscopic collision events such that the radial velocity component is reset to $V_r = 0$ following each ion-neutral collision [32]. In this case, if a constant electric field is present, the net velocity (or drift velocity) that arises from the microscale events is constant while changes in the magnitude of the drift velocity are directly proportional to the changes in the magnitude of the electric field (when other variables such as P and q are constant). Furthermore, the drift velocity and electric field vectors are in the same direction for a positively charged ion. Mathematically, for the sinusoidally changing acceleration caused by the force in Eq. (11), the radial velocity, V_r, profile in the *low-field* collisional regime may be obtained by the drift velocity as,

$$V_r = KE_{0,r} \sin\frac{2\pi V_z}{\lambda} t \tag{15}$$

where K is the ion mobility coefficient.

By integrating Eq. (15) with respect to t, the radial displacement, r, can be obtained,

$$r = -KE_{0,r} \frac{\lambda}{2\pi V_z} \cos\frac{2\pi V_z}{\lambda} t + r_i \tag{16}$$

where r_i is the initial *r*-position. It is important to note that Eq. (16) describes the effective RF motion in the presence of ion-neutral collisions assuming constant $E_{0,r}$ and V_z. However, as *r*-position increases, $E_{0,r}$ increases as shown in Fig. 3(b). As *z*-position increases, V_z oscillates according to E_z and n [8]. Each effect induces changes in both the amplitude and the frequency of the motion described by Eq. (16). The amplitude changes may be considered symmetric in the (+) and (−) *r* segments of the radial ripple motion while the frequency changes are not observed in the final ion trajectory traces since they are displayed in the space domain with fixed λ.

[1] Reference [8] contains a typographical error in discussion of the effective RF wavelength. In the PDC IG, a single electrode subunit represents *one* effective RF wavelength, as depicted here in Fig. 3(b).

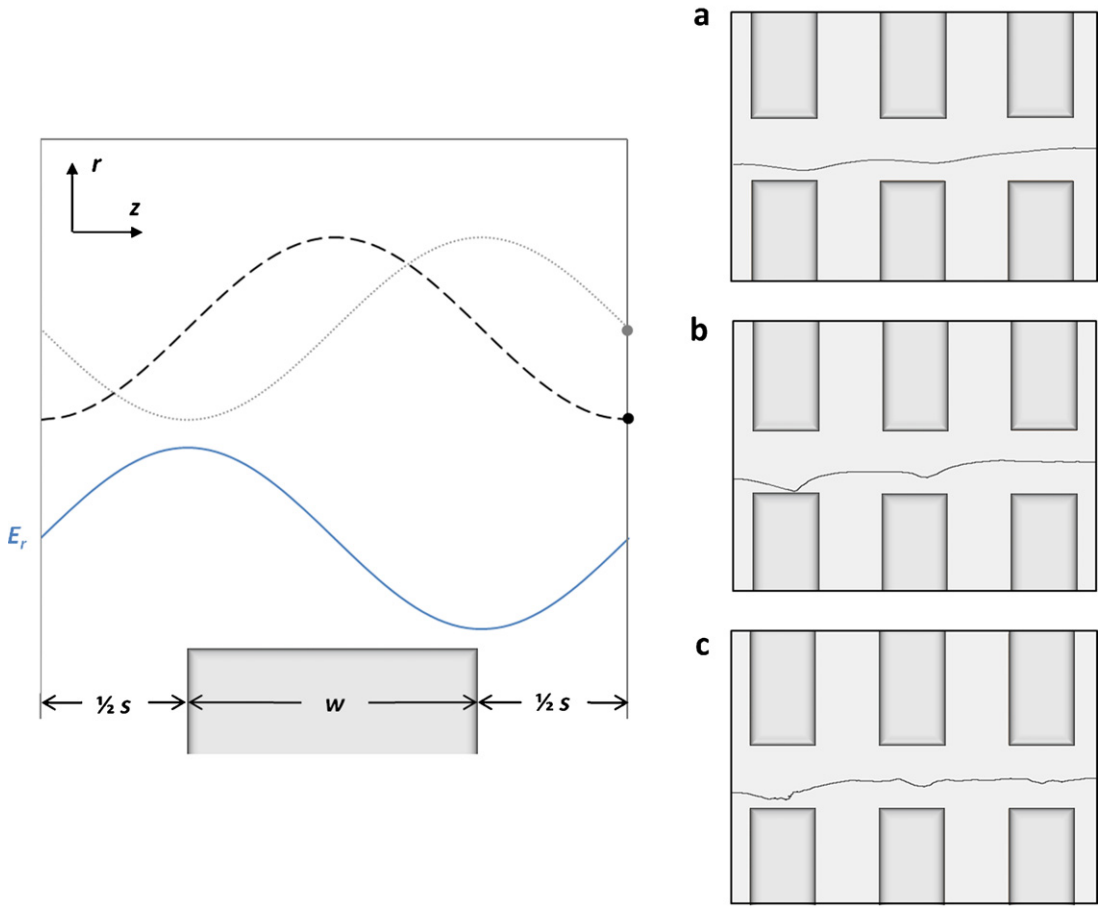

Fig. 4. Left panel: Ion motion in the radial direction for vacuum (dotted grey line) and in the presence of thermalizing collisions (dashed black line) for one periodic focusing subunit as predicted by Eqs. (14) and (16), respectively for the static radial electric field represented below by the solid blue line. Motion due to initial radial velocity is neglected for the trajectory shown for vacuum conditions. The maximum ion displacement in the *r*-dimension is shifted in phase by 90° between collisional and non-collisional boundary regimes. Right panel: Simulation of an ion trajectory starting at $r = 1.5$ mm at E_c/N 150 (a), 75 (b), and 37 (c) Td. In each case, three discrete transport modes described in Section 3.1 are present. Maximum *r*-displacement occurs between the tailing electrode edge and the midpoint inside electrodes as predicted by Eqs. (14) and (16), respectively. (For interpretation of the references to color in this figure legend, the reader is referred to the web version of the article.)

More importantly, Eq. (16) assumes that ion kinetic energy is reset to zero following subsequent collision events. In other words, the radial momentum of the ion is completely damped during the collisions. However, reference [8] clearly demonstrates that T_{eff} oscillates about an average value greater than the temperature of the bath gas, *T*. Therefore, under stable operating conditions, ions in the PDC IG maintain a fraction of their initial radial momentum after a collision event with a neutral gas molecule which is consistent with IMS in an *intermediate field*. Thus, the results of the previous derivation (Eqs. (14) and (16)) represent the two boundary conditions for the PDC IG and are depicted in Fig. 4 (left panel). The inclusion of *K* in Eq. (16) indicates that the amplitude of radial motion has a dependency on mobility and may contribute to defining a low-mobility limit for PDC IG. However, further investigation into this phenomenon is outside of the scope of this work, but is currently being investigated.

During stable operation of the PDC IG, maximum radial displacement (corresponding to the ion turnaround point) is dependent upon E/N as depicted by the simulations shown in Fig. 4 (right panel) for several conditions obtained by varied pressure. Note that the left panel in Fig. 4 shows boundary-condition ion motions in the upper half of the PDC IG while the simulations in the right panel shows ion trajectories in the bottom half (inverted across the $r = 0$ plane with respect to the former). Fig. 4 shows that at higher E/N, ion turnaround point resembles the vacuum expression given by Eq. (14) which predicts that the ion turnaround point is at the tailing edge of the electrode. Conversely, at lower E/N, the ion turnaround point occurs near the midpoint of the electrode which is predicted by Eq. (16). Thus, the simulations contained in the right panel of Fig. 4 are in agreement with the concept that the radial ion motion predicted by Eqs. (14) and (16) represent the two boundary conditions where the radial momentum of the ion is conserved (Eq. (14)) and completely damped (Eq. (16)).

3.4. The effective potential model

Although the radial ripple motion is clear from Fig. 2, slow drift about $r = 0$ is slightly less obvious in a single periodic-focusing subunit, though easily observed after several effective RF cycles. In reference [8], we attributed this central drift motion phenomenon to effective potentials created by the electric field variations and collisional cooling. The theoretical basis for the estimation of effective potentials is provided by the presence of fast (kHz) and continuous effective RF with increasing amplitude in the (+) *r*-direction as shown in Fig. 3(b). Without considering the damping effects by the buffer gas (and the changes in $E_r(r)$ or V^* decay profiles in the *z*-dimension as discussed later), the effective potentials in a PDC IG, V^*, may be represented by the expression [8]:

$$V^* = \frac{q^2 E_{0,r}(r)^2}{4m\Omega_{eff}{}^2} \tag{17}$$

The conservation of the radial momentum, at least to some extent, is vital for the effective potential concept. Let us first consider an undamped effective potential model as represented by Eq. (17). While the mathematical treatment for the undamped effective potential model is well established, a qualitative physical description of the origin of effective potentials in the PDC IG (considering no damping) may be presented contemplating the conserved momentum of a positively charged ion. Consider an ion initially residing at a certain r-position and traveling in the z-direction. During its z-motion, the ion is subjected to different phases of the $E_r(z)$ waveforms, *i.e.*, the ion *sees* an effective RF. When the phase is (+), the ion is subjected to a force in the (+) r-direction (away from $r = 0$, (+) force), while the (−) phase applies a force in the (−) r-direction (towards $r = 0$, (−) force). Consider an ion moving in the (+) r-direction under the influence of a (+) phase. Consequently, the ion is subjected to waveforms having higher amplitudes that impart progressively higher (+) force. After the ion reaches the z position where the waveforms switch to (−) phase, a (−) force is exerted on the ion. However, at the transition point, the ion has already acquired a momentum in the (+) r-direction and thus the ion has to be decelerated by the (−) force before it turns around. Thus, a certain turnaround time results in the ion traveling an additional distance in (+) r-direction from the time it is subjected to the waveform phase change. Let us term this extra displacement in the r-direction the turnaround displacement. After turning around, the ion travels in the (−) r-direction and is subjected to (−) phase waveforms that apply progressively lower (−) force due to decreasing amplitudes. Subsequently, the ion reaches the z-position where the waveforms change phase to (+) again, applying a (+) force on the ion. By this time, the ion has acquired momentum in the (−) r-direction. However, unlike in the previous turnaround event, the waveforms have lower amplitudes and do not apply a force as high as the previous scenario during deceleration. This causes the ion to have a longer turnaround displacement in the (−) r-direction than in the previous scenario. Due to this, the ion also displaces in the (−) r-direction beyond the initial r-position. Over several RF cycles, the net effect of this displacement is seen as an apparent drift towards the $r = 0$ position, which is here suggested as the physical origin of the effective potentials.

Since the effective RF motion of the ions under stable operating parameters in a PDC IG represents an intermediate situation between the completely conserved radial momentum (Eq. (14)) and completely damped radial momentum (Eq. (16)), the central drift motion may be explained using a damped effective potential model. To a first approximation, the damping of V^* with respect to Eq. (17) may considered to be by a uniform factor throughout the device since the number density of the buffer gas, N, is uniform under constant static pressure conditions. In other words, although a finite portion of the ion radial momentum is damped, an undamped portion remains conserved, defining an adiabatic total energy. This may give rise to effective potentials damped by a factor with respect to the magnitudes predicted by Eq. (17). According to this approximation, the relative magnitudes of the effective potential profiles remain the same as presented in reference [8] with relatively higher magnitudes towards the tailing edge of the electrode as a result of the low axial ion velocities in that region. Accordingly, Fig. 5 contains a flowchart of the proposed PDC IG focusing mechanism on the basis of a damped V^*. The bottom panel of Fig. 5 contains a 3D profile of effective potentials that result in the radial ion confinement.

Although the ion-neutral collisions damp the effective potentials, the presence of collisions is vital for the focusing mechanism to take effect. This is illustrated by the fact that the radial ripple and central drift motion are largely absent under vacuum conditions (simulation not shown) or dominant axial electric field conditions in the presence of collisions, *i.e.*: the gap between adjacent electrodes. The latter is demonstrated by the fact that detailed motion due to the radial electric field is not observed in Fig. 4 (right panel) near the leading and tailing edges of the electrodes and in the spacing between the electrodes because the axial electric field is dominant in these regions. Under these conditions, the ions are mainly influenced by the larger axial fields acquiring a relatively large V_z. In this case, ions do not spend sufficient time inside the electrodes to follow a well-defined radial ripple motion under the influence of the radial fields. More specifically, an increase in the axial ion velocity increases Ω_{eff} (Eq. (10)) causing an instantaneous decrease in the amplitude of the radial ripple motion (Eqs. (14) and (16)). In the presence of collisions, ion momentum is dampened such that ion axial velocity decreases inside the electrodes and ion motion may be influenced by the relatively weak radial electric fields to follow the radial effective RF motion, giving rise to damped effective potentials. In other words, collisional damping is vital in radial focusing. Our simulations also indicated a low molecular weight inert gas such as He produces smoother effective RF trajectories in contrast to higher molecular weight gases such as N_2 that cause scattering. This phenomenon is similar to the trapping of ions by means of smooth secular motion in a quadrupolar ion trap where the optimum performance in terms of resolution is obtained when He is used for collisional damping [33].

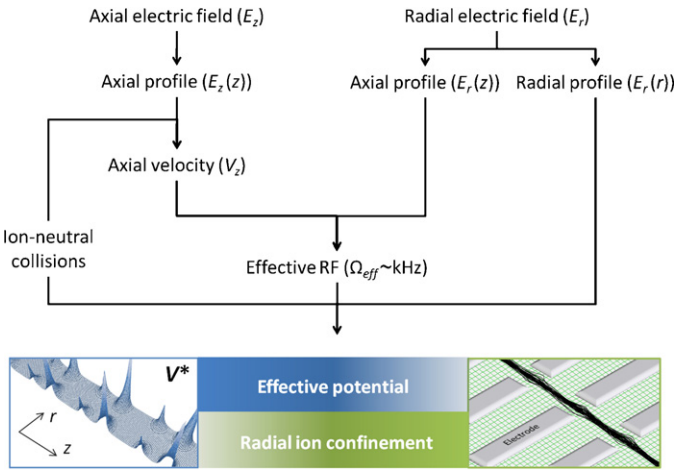

Fig. 5. Flowchart diagram of the proposed radial focusing mechanism in the PDC IG.

Unlike in traditional RF devices, $V^*(r)$ profiles are composed of a combination of multipole terms that are different for each z-position. The exponentially decaying $V^*(r)$ profile expected for a thin ring electrode is observed only at the edges of the electrodes [8] while the fringing fields create different combinations of multipole $V^*(r)$ profiles at other z-positions. However, our modeling of $E_r(z)$ waveforms as sinusoidal functions presumably already takes into account the said variations. The $1/\Omega_{eff}$ term signifies the amount of time the ion spends at each z-position. For example, the middle of the electrode (region C, as denoted in reference [8]) contains very small $E_r(r)$ variations while the $1/\Omega_{eff}$ term is relatively large. These conditions create a region where the effective potentials are minimal or absent. The incorporation of an n-dependent damping factor into Eq. (17) may explain this phenomenon. We previously showed that for relatively low E/N conditions (<37 Td), ion losses may occur in the middle of each electrode, supporting the adopted V^* representation. In this region, V^* creates a potential well in the axial dimension (Fig. 5, bottom panel) and ions without sufficient axial velocity may be lost towards the electrode walls by either diffusion or radial electric fields. Increasing w beyond a certain limit will convert this region to a field-free diffusing region. Similar potential wells have been reported by Giles et al. for a traveling wave ion mobility spectrometer with an RF applied 180° out-of-phase to

adjacent electrodes and a superimposed DC pulse that travels in the z-dimension [7].

The fast effective RF motion can be decoupled from the slower central drift motion as shown in the simulations, suggesting that the first order adiabatic approximation [11] used in deriving Eq. (17) may still be used for the estimation of V^*. Additionally, the fact that the magnitude of radial electric field variations (dE_r/dr) during one effective RF cycle is small compared to the magnitude of the radial electric field, provides justification for the use of an adiabatic approximation. However, the presence of collisional damping and the z-dependence of the $V^*(r)$ profiles complicate a quantitative calculation or validation of the effective potentials for PDC IG. In other words, the use of adiabatic approximations to validate a V^* model damped with respect to Eq. (17) or a model that incorporates the z-dependence of $V^*(r)$ is beyond the scope of the current study. The model is presented in order to provide a semi-quantitative understanding of the effective potentials in a PDC IG and an exact mathematical treatment of V^* is not intended.

3.5. Axial ion transport: ion mobility in a periodic-focusing electric field

IMS separation in the PDC IG is affected by two different phenomena: (1) periodic changes in the electric field and (2) periodic changes in the number of collisions per unit z-displacement, n, initiated by the electric field variations [8]. In this section, ion mobility separation in a periodic-focusing electric field is discussed while the effect of n is addressed in the subsequent section.

It is important to realize that a potential drop across a thick periodic-focusing electrodes of aspect ratio s:w:d gives rise to a non-linear axial electric field (E_z). In this section, only the variations in the axial electric field in the axial direction ($E_z(z)$) and radial direction ($E_z(r)$) are considered since only E_z is relevant to the discussion of IMS separation. Let us also consider PDC IG designs with two different aspect ratios: PDC $IG_{1:1:1}$ and PDC $IG_{3:3:4}$. Fig. 6(a) contains plots of ($E_z(z)$) at $r=0$ for both geometries normalized to the PDC $IG_{1:1:1}$. For each lens configuration $E_z(z)$ closely approximates a sinusoidal function. Thus, as ions traverse the device in the z-direction at a constant r-position, the electric field oscillates about a central electric field, E_c, where the amplitude of the sinusoidal function is denoted as E_0. The maximum $E_z(z)$ at $r=0$ (equivalent to E_c+E_0) is located at the midpoint between adjacent electrodes whereas the minimum $E_z(z)$ (equivalent to E_c-E_0) is located at the mid-point inside electrodes. The value of E_c may be obtained from,

$$E_c = \tfrac{1}{2}(E_{max} + E_{min}) \tag{18}$$

Fig. 3(a) shows that in the (+) r-direction, the shape of $E_z(z)$ deviates from the sinusoidal waveform observed at $r=0$, while the spatial periodicity (wavelength) and phase of the electric field remain constant. At the electrode inner surface ($r_{surface}$) $E_z(z)$ may be approximated by a square wave, although variations are observed near the electrode inner edges. For the approximated $E_z(z)$ square waveform at $r_{surface}$, the maximum value is located in the gap between adjacent electrodes which approximates the maximum electric field that exists between the walls of two adjacent electrodes beyond the central orifice ($r > r_{surface}$). However, for the approximated $E_z(z)$ square waveform at $r_{surface}$, the minimum value is located on the inner electrode surface and is always zero. These outcomes imply that $r_{surface}$ contains the boundary conditions for E_{max} and E_{min} values. Fig. 3(a) also demonstrates that in the (+) r-direction, E_{min} shifts towards the minimum boundary condition more rapidly than E_{max} shifts towards the maximum boundary condition. Mathematically, this outcome may be stated,

$$\left|\frac{d(E_{\max})}{dr}\right| < \left|\frac{d(E_{\min})}{dr}\right| \tag{19}$$

which is a consequence of the fact that while the boundary condition for E_{max} is determined only by the voltage difference between adjacent electrodes of spacing s, the boundary condition for E_{min} is always fixed at zero. As a result of Eq. (19), E_c, decreases in the (+) r-direction as reflected in Fig. 6(b) for PDC $IG_{1:1:1}$ and PDC $IG_{3:3:4}$ configurations. The importance of $E_c(r)$ is considered later in the context of diffusion-limited IMS expressions.

Nevertheless, in any IMS separation, if the required *low*- or *intermediate*-field conditions [28] are maintained, the changes in the electric field do not change K since the drift time in Eq. (1) is inversely proportional to E. For the PDC IG, the position-varying electric field conditions may also be represented by a net electric field ($\bar{E}$) obtained by integrating over the periodic axial electric field profile. That is, for a fixed r position, the axial mobility separation can be described by replacing E in Eqs. (1) and (6) with $\bar{E}$. In order to derive an expression for $\bar{E}$, let us consider an ion traveling in the (+) z-direction at the $r=0$ position. The spatial periodicity (wavelength) of the axial electric field is given by λ in Eq. (9). The spatial variation of the axial electric field may be described by,

$$E_z(z) = E_0 \ \cos(\omega_z z) + E_c \tag{20}$$

where,

$$\omega_z = \frac{2\pi}{\lambda} \tag{21}$$

such that,

$$E_z(z) = E_0 \ \cos\left(\frac{2\pi z}{\lambda}\right) + E_c \tag{22}$$

Owing to the periodicity of the $E_z(z)$ waveform, the net electric field resulting at $r=0$ can be obtained by integrating over one wavelength,

$$\bar{E} = \int_0^{2\pi} \left[E_0 \cos\left(\frac{2\pi z}{\lambda}\right) + E_c\right] dz \tag{23}$$

yielding,

$$\bar{E} = E_c \tag{24}$$

Thus, for ions traveling in the (+) z-direction at constant r position, the net electric field that contributes to the overall mobility separation is identical to a uniform electric field with the magnitude E_c. In this case, the mobility coefficient and the resolution in the PDC IG are explained by Eqs. (1) and (6) with E substituted by E_c as follows,

$$K = \frac{L}{t_d E_c} \tag{25}$$

$$R = \frac{t_d}{\Delta t_d} = \frac{1}{4}\left(\frac{qLE_c}{K_B T \ \ln 2}\right)^{1/2} \tag{26}$$

Eqs. (25) and (26) accurately provide the mobility coefficient and the diffusion-limited resolution for ions traveling along the z-dimension at $r=0$ position in the PDC IG. However, ions traversing in the PDC IG drift to different radial positions (owing to radial ripple motion and diffusion) although being periodically refocused towards the $r=0$ position (by effective potentials). Ion optics simulations [8,9] suggest that ions at initial $r \neq 0$ positions are focused to the $r=0$ position after traversing a few electrodes (~1–4, depending on the initial ion position, E/N, and w:s:d), and that overall ion migration to r-positions exceeding half the value of the radius ($r=0.25d$) is extremely rare. For both electrode configurations, at $r<0.25d$, the deviation in E_c from E_c ($r=0$) is minimal (<2%), as shown in Fig. 6(b). Thus, assuming E_c ($r<0.25d$) $\approx E_c(r=0)$, Eqs. (25) and (26) can still provide a practical estimate of the overall theoretical (diffusion-limited) K and R in the PDC IG. Moreover, Fig. 6(b)

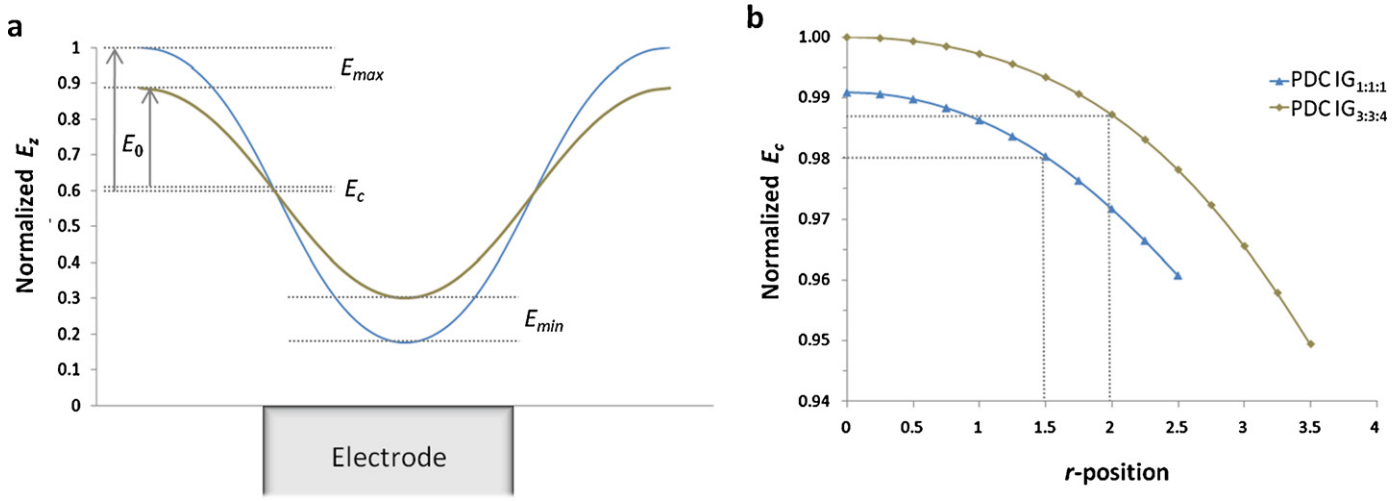

Fig. 6. (a) Axial electric field at the $r = 0$ position for the PDC $IG_{1:1:1}$ (blue, curve with larger E_0) and PDC $IG_{3:3:4}$ (tan) electrode configurations. The electric field is shown with respect to electrode position and normalized to the maximum value. (b) Central electric field as a function of r-position shown for both PDC $IG_{1:1:1}$ (blue ▲) and PDC $IG_{3:3:4}$ (tan ♦). Data is shown normalized to the PDC $IG_{3:3:4}$ E_c ($r = 0$) curve. The vertical dotted lines denote the r-position at half-radius ($r = 0.25d$) for both electrode configurations. In each case, E_c ($r = 0.25d$) corresponds to <2% decrease from E_c ($r = 0$) as indicated by the horizontal dotted lines. (For interpretation of the references to color in this figure legend, the reader is referred to the web version of the article.)

shows that as d is increased, $E_c(r = 0)$ increases which is accompanied by a decrease in the amplitude of the E_c waveform shown in Fig. 6(a). In this case, the resulting electric field near the central z axis exhibits fewer r- and z-variation which ultimately increases the measurement resolution as observed in the experimental data discussed below. Finally, as d becomes sufficiently large, the electric field near the z-axis approaches a uniform electric field with the magnitude of the applied electric field, E, as in DT IMS. In other words, for large d values, the amplitude term of the $E_z(z)$ at $r = 0$ waveform approaches zero while E_c approaches E. Therefore, as d is increased, the resolution of the IMS measurement increases; however, as detailed in references [8,9], the ion transmission through the device will decrease. Moreover, R in the PDC IG can be increased without affecting ion transmission by simply increasing the length (L) while keeping the applied electric field constant according to Eq. (26) and data presented in reference [9]. Thus, PDC IG has utility as a high ion transmission and high resolution gas phase ion separation device that is based on first-order IMS principles.

3.6. "Mobility Damping" approach

Apart from the unique electric field, PDC IG has several other novel features-one being the number of ion neutral collisions per unit z-displacement (n). In the PDC IG, n oscillates in the z-dimension, initiated by low axial electric fields inside of electrodes. As explained earlier, when the axial electric field is low inside of electrodes, the radial electric fields influence ion motion to a greater extent which increases the amplitude of the radial ripple motion and thus, the distance traversed inside of an electrode. The overall result is that n increases inside of electrodes even though the collision frequency has decreased (owing to low V_z) while the number density of the buffer gas, N, remains constant. In this section, the collective effects of E and n variations on ion mobility in the PDC IG are discussed.

When the calculation of Ω is desired, the measurement accuracy of K becomes increasingly important. The K value obtained by Eq. (25) approaches the best case scenario according to the assumption that the damping in the net electric field with reference to the applied electric field caused by the ion migration to different radial positions is negligible and that the changes to the measured drift time caused by periodic increases in n are negligible. However, the periodic increases to n (with respect to uniform field conditions where n is constant) increases the drift time causing the measured apparent mobility to be lower than the actual K. The overall effect of ions being subjected to varying electric field and n may be described as if an ion subjected to a net E/n ratio that is lower with respect to a uniform electric field where the ratio E/n is constant. Note that the term E/n is used here in place of more common term E/N since the periodic changes of n are initiated by changing electric fields, and are not due to changes in N which is constant. With this approach, a more accurate description of mobility in a PDC IG may be presented by assuming that the net apparent mobility decrease can be quantified by using a correction term with reference to uniform electric field conditions. The correction term, termed the mobility damping coefficient, α, is introduced into Eq. (1) such that,

$$K = \frac{L}{t_D \alpha E} \tag{27}$$

and the collision cross section may be obtained by,

$$\Omega = \left(\frac{3q}{16N_0}\right)\left(\frac{2\pi}{\mu K_B T}\right)^{1/2}\left(\frac{t_D \alpha E}{L}\right)\left(\frac{P_0 T}{P T_0}\right) \tag{28}$$

Note that Eqs. (27) and (28) are equivalent to Eqs. (1) and (5), respectively, for $\alpha = 1$, which corresponds to the absence of mobility damping (or more simply, DT IMS conditions). In deriving Eq. (28), potential impacts on the ion 3D structure due to periodic annealing and cooling introduced by the variation of T_{eff} is assumed to be negligible. Moreover, for a given drift tube design, and N, determination of α yields a constant value neglecting a potential analyte dependence (which is currently being investigated). That is, at constant N for a given electrode geometry, the net electric field ions are subjected to is damped by a constant factor with respect to the applied field. Thus, α can be defined as:

$$\alpha = \frac{K_{\text{PDC IG}}}{K_{\text{DT IMS}}} = \frac{K_{0,\text{PDC IG}}}{K_{0,\text{DT IMS}}} \tag{29}$$

Furthermore, as d is increased, α increases and approaches unity (DT IMS conditions). In this respect, the electric field damping approach underscores the relationship between the PDC IG variables and DT IMS.

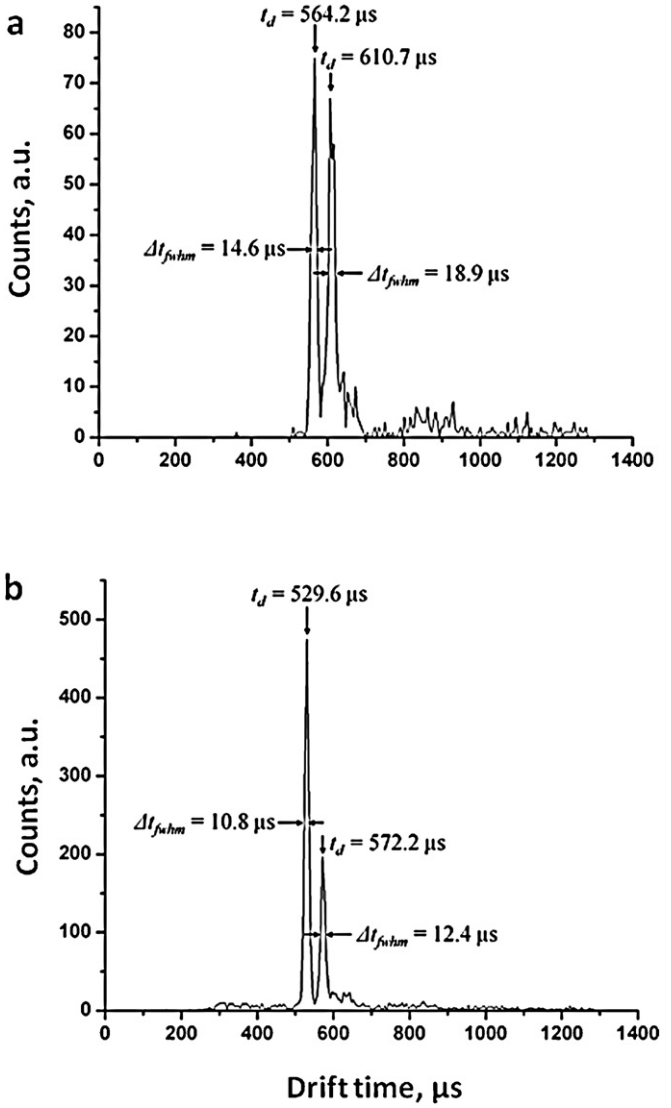

Fig. 7. Drift time spectra for fullerenes on 63 cm PDC IG drift tubes with two electrode configurations: (a) in PDC $IG_{1:1:1}$ (s:w:d = 6 mm), (b) in PDC $IG_{3:3:4}$ (s:w = 6 mm, d = 8 mm). Data were obtained ~1.5 Torr. Measured resolutions for C_{60} and C_{70} for (a) are 39 and 32 while those for (b) are 49 and 46, respectively.

3.7. Experimental IMS resolution and determination of collision cross section

Ion mobility spectra obtained for fullerenes for two different PDC IG electrode configurations are shown in Fig. 7. Experimental conditions and the measured quantities such as the drift times and the mobility resolution are reported in the figure and the experimental section. The data indicates that the measured resolution obtained for the PDC $IG_{3:3:4}$ is higher than the PDC $IG_{1:1:1}$ under a constant set of experimental conditions and in good agreement with the theoretical explanation provided above, where higher resolution is expected when d is increased. Maximum resolution obtained in these experiments is ~50 for the PDC $IG_{1:1:1}$ and ~60 for the PDC $IG_{3:3:4}$, although calculation of diffusion-limited resolution by Eq. (26) predicts an upper limit of ~100 for both designs for the experimental conditions employed. Although the experimental resolutions reported here are high relative to values routinely reported for IMS, they are considerably lower than the theoretical upper limit predicted by Eq. (26) for several reasons including differences in the initial kinetic energy and spatial spreads of the ions as well as radial motion contributing to α.

For the determination of accurate collision cross section, α can be determined using a compound of known Ω (calibrant) for the subsequent calculation of Ω for an unknown analyte under the same experimental conditions. Considering potential analyte effects, the calibrant may be chosen so that it belongs to the same chemical class and is similar to the analyte in terms of Ω and m. However, when α/P is not known, it is also possible to empirically determine the ratio α/P using a calibrant for the calculation of unknown Ω under the same experimental conditions. In other words, a simple calibration method yields accurate Ω following DT IMS principles. Here, the Ω for $C_{60}^{\bullet+}$ (124 Å^2) [34,35] was used to calculate a calibration constant, α/P yielding $\Omega = 134 \pm 5$ Å^2 for $C_{70}^{\bullet+}$ which is in agreement with our DT IMS measurements that provided $\Omega = 138 \pm 1$ Å^2 for $C_{70}^{\bullet+}$ [36]. Sawyer et al. obtained Ω values for the conformations of bradykinin fragment 1-5 using a similar calibration procedure for PDC IG assuming first-order IMS principles using bradykinin as a calibrant [30]. The results were in agreement with theoretically obtained Ω values. More experiments are currently underway to study the dependence of α on N and the analyte, to produce collision cross section values for peptides using PDC IG and evaluate the accuracy of the measurements with respect to DT IMS using the principles derived herein.

4. Conclusions

Under stable operation of the PDC IG, three dominant ion motions are observed: axial motion, radial ripple, and a central drift motion. The overall radial ion confinement is a result of the central drift motion which acts in the (−) r-direction. However, under vacuum conditions, axial motion dominates which suggests that collisional cooling is required for ions to access weaker radial field components that give rise to radial ripple (due to effective RF) and central drift motion (due to a damped effective potential). This result leads to a convoluted interpretation of the adiabatic approximation since the criteria are interpreted under vacuum conditions while commonly used under pressure conditions for RF devices. Although all three drift motions are clearly observed for all stable E/N conditions, a limitation of the current effective potential theory is that a straightforward mathematical means of first-order verification is not provided in the presence of collisional cooling. While this outcome complicates the theoretical treatment for adiabaticity, herein lies one of several unique analytical advantages of the PDC IG: the periodic-focusing field generates the radial ion confinement which conventionally requires superimposed DC and RF potentials.

Moreover, ion mobility expressions for the PDC IG yield results similar to DT IMS *via* calculation of a mobility damping coefficient α, which can be readily determined for a fixed PDC IG design. While the PDC IG produces high ion transmission, a modest decrease in resolution is observed compared to DT IMS; however, the decrease in resolution can be overcome by simply increasing the drift length without affecting ion transmission. Note that under stable operating conditions, ions are not lost at the electrode surface and ion transmission through the device is only governed by the size of the exit aperture to the detector or MS analysis stage. Finally, calculation of K and Ω in the PDC IG can be achieved through first-order expressions similar to DT IMS.

Acknowledgements

The authors would like to thank Dr. Melvin A. Park and Dr. Francisco Fernandez-Lima for their helpful correspondence, Will Seward and Carl Johnson of the Texas A&M Machine Shop for

fabrication of all custom instrumentation, Greg Matthijetz for his electronics expertise, as well as Al Schultz and Tom Egan of Ionwerks, Inc. (Houston, TX) for the data acquisition system used in this work. The National Science Foundation—Major Research Instrumentation Program DBI-0821700 and the Department of Energy, Division of Chemical Sciences, BES DE-FG02-04ER15520 supported this work.

References

[1] B.K. Bluhm, K.J. Gillig, D.H. Russell, Development of a Fourier-transform ion cyclotron resonance mass spectrometer-ion mobility spectrometer, Rev. Sci. Instrum. 71 (2000) 4078–4086.
[2] S.L. Koeniger, S.I. Merenbloom, S.J. Valentine, M.F. Jarrold, H.R. Udseth, R.D. Smith, D.E. Clemmer, An IMS-IMS analogue of MS-MS, Anal. Chem. 78 (2006) 4161–4174.
[3] K.J. Gillig, D.H. Russell, Periodic field focusing ion mobility spectrometer, US Patent 6,639,213 B2 (2003).
[4] K.J. Gillig, B.T. Ruotolo, E.G. Stone, D.H. Russell, An electrostatic focusing ion guide for ion mobility-mass spectrometry, Int. J. Mass Spectrom. 239 (2004) 43–49.
[5] K. Thalassinos, S.E. Slade, K.R. Jennings, J.H. Scrivens, K. Giles, J. Wildgoose, J. Hoyes, R.H. Bateman, M.T. Bowers, Ion mobility mass spectrometry of proteins in a modified commercial mass spectrometer, Int. J. Mass Spectrom. 236 (2004) 55–63.
[6] A.A. Shvartsburg, R.D. Smith, Fundamentals of traveling wave ion mobility spectrometry, Anal. Chem. 80 (2008) 9689–9699.
[7] K. Giles, S.D. Pringle, K.R. Worthington, D. Little, J.L. Wildgoose, R.H. Bateman, Applications of a travelling wave-based radio-frequency-only stacked ring ion guide, Rapid Commun. Mass Spectrom. 18 (2004) 2401–2414.
[8] J.A. Silveira, C.M. Gamage, R.C. Blase, D.H. Russell, Gas-phase ion dynamics in a periodic-focusing DC ion guide, Int. J. Mass Spectrom. 296 (2010) 36–42.
[9] R.C. Blase, J.A. Silveira, K.J. Gillig, C.M. Gamage, D.H. Russell, Increased ion transmission in IMS: a high resolution, periodic-focusing DC ion guide ion mobility spectrometer, Int. J. Mass Spectrom. (2010), doi:10.1016/j.ijms.2010.08.016.
[10] H.G. Dehmelt, Radiofrequency spectroscopy of stored ions—I: Storage, Adv. At. Mol. Phys. 3 (1967) 53–72.
[11] D. Gerlich, State-Selected and State-to-State Ion-Molecule Reaction Dynamics Part 1. Experiment, vol. LXXXII, John Wiley & Sons, Inc., 1992, pp. 1–176.
[12] S. Guan, A.G. Marshall, Stacked-ring electrostatic ion guide, J. Am. Soc. Mass Spectrom. 7 (1996) 101–106.
[13] M.F. Jarrold, V.A. Constant, Silicon cluster ions: evidence for a structural transition, Phys. Rev. Lett. 67 (1991) 2994–2997.
[14] D.E. Clemmer, M.F. Jarrold, Metal-containing carbon clusters: structures, isomerization, and formation of NbCn+ clusters, J. Am. Chem. Soc. 117 (1995) 8841–8850.
[15] P. Dugourd, R.R. Hudgins, J.M. Tenenbaum, M.F. Jarrold, Observation of new ring isomers for carbon cluster anions, Phys. Rev. Lett. 80 (1998) 4197–4200.
[16] G. von Helden, M.-T. Hsu, P.R. Kemper, M.T. Bowers, Structure of carbon cluster ions from 3 to 60 atoms: linears to rings to fullerenes, J. Chem. Phys. 95 (1991) 3835–3837.
[17] G. von Helden, P.R. Kemper, N.G. Gotts, M.T. Bowers, Isomers of small carbon cluster anions: linear chains with up to 20 atoms, Science 259 (1993) 1300–1302.
[18] E.R. Brocker, S.E. Anderson, B.H. Northrop, P.J. Stang, M.T. Bowers, Structures of metallosupramolecular coordination assemblies can be obtained by ion mobility spectrometry-mass spectrometry, J. Am. Soc. Mass Spectrom. 132 (2010) 13486–13494.
[19] P. Weis, P.R. Kemper, M.T. Bowers, Structures and energetics of Vn(C_6H_6)m+ clusters: evidence for a quintuple-Decker sandwich, J. Phys. Chem. A 101 (1997) 8207–8213.
[20] R.R. Hudgins, M.F. Jarrold, Helix formation in unsolvated alanine-based peptides: helical monomers and helical dimers, J. Am. Chem. Soc. 121 (1999) 3494–3501.
[21] R.R. Hudgins, M.F. Jarrold, Conformations of unsolvated glycine-based peptides, J. Phys. Chem. B 104 (2000) 2154–2158.
[22] G.A. Breaux, M.F. Jarrold, Probing helix formation in unsolvated peptides, J. Am. Chem. Soc. 125 (2003) 10740–10747.
[23] D.E. Clemmer, R.R. Hudgins, M.F. Jarrold, Naked protein conformations: cytochrome c in the gas phase, J. Am. Chem. Soc. 117 (1995) 10141–10150.
[24] K.B. Shelimov, M.F. Jarrold, Conformations, unfolding and refolding of apomyoglobin in vacuum: an activation barrier for gas-phase protein folding, J. Am. Chem. Soc. 119 (1997) 2987–2994.
[25] K.B. Shelimov, D.E. Clemmer, R.R. Hudgins, M.F. Jarrold, Protein structure in vacuo: gas-phase conformations of BPTI and cytochrome c, J. Am. Chem. Soc. 119 (1997) 2240–2248.
[26] R.R. Hudgins, J. Woenckhaus, M.F. Jarrold, High resolution ion mobility measurements for gas phase proteins: correlation between solution phase and gas phase conformations, Int. J. Mass Spectrom. Ion Processes 165–166 (1997) 497–507.
[27] N.P. Nelson, P. Barrera, N.D. Bartolo, P.J. Booth, C.V. Robinson, Micelles protect membrane complexes from solution to vacuum, Science 321 (2008) 243–246.
[28] E.A. Mason, E.W. McDaniel, Transport Properties of Ions in Gases, John Wiley & Sons, Inc., 1988.
[29] T. Wyttenbach, G. von Helden, M.T. Bowers, Gas-phase conformation of biological molecules: bradykinin, J. Am. Chem. Soc. 118 (1996) 8355–8364.
[30] H.A. Sawyer, J.T. Marini, E.G. Stone, B.T. Ruotolo, K.J. Gillig, D.H. Russell, The structure of gas-phase bradykinin fragment 1-5 (RPPGF) ions: an ion mobility spectrometry and H/D exchange ion-molecule reaction chemistry study, J. Am. Soc. Mass Spectrom. 16 (2005) 893–905.
[31] R.E. March, J.F.J. Todd, Quadrupole Ion Trap Mass Spectrometry, second edition, John Wiley & Sons, Inc., 2005.
[32] A.A. Shvartsburg, Differential Ion Mobility Spectrometry, Nonlinear Ion Transport and Fundamentals of FAIMS, CRC Press, 2009.
[33] R.M. Danell, A.S. Danell, G.L. Glish, R.W. Vachet, The use of static pressures of heavy gases within a quadrupole ion trap, J. Am. Soc. Mass Spectrom. 14 (2003) 1099–1109.
[34] G. von Helden, T. Wyttenbach, M.T. Bowers, Inclusion of a MALDI ion source in the ion chromatography technique: conformational information on polymer and biomolecular ions, Int. J. Mass Spectrom. Ion Processes 146–147 (1995) 349–364.
[35] T. Wyttenbach, G. von Helden, J.J.J. Batka, D. Carlat, M.T. Bowers, Effect of the long-range potential on ion mobility measurements, J. Am. Soc. Mass Spectrom. 8 (1997) 275–282.
[36] J.A. Silveira, C.M. Gamage, D.H. Russell, A periodic-focusing DC ion funnel interface for a variable-temperature ion mobility spectrometer, 59th ASMS conference on mass spectrometry and allied topics, 2011, Abstract submitted.